Journal of Orthopaedic Translation 50 (2025) 144–157

Contents lists available at ScienceDirect

Journal of Orthopaedic Translation

journal homepage: www.journals.elsevier.com/journal-of-orthopaedic-translation

Original Article

Moderate static magnetic field regulates iron metabolism and salvage bone loss caused by iron accumulation

Chenxiao Zhen [a,b,c], Shenghang Wang [d], Jiancheng Yang [e], Gejing Zhang [a,b,c], Chao Cai [a,b,c], Jianping Wang [a,b,c], Aifei Wang [f], Youjia Xu [f], Yanwen Fang [g], Min Wei [g], Dachuan Yin [a,c], Xinle Luo [d], Ming Gong [d], Hao Zhang [d], Peng Shang [b,c,*]

[a] School of Life Sciences, Northwestern Polytechnical University, Xi'an, 710072, China
[b] Research & Development Institute of Northwestern Polytechnical University, Shenzhen, 518057, China
[c] Key Laboratory for Space Bioscience and Biotechnology, Institute of Special Environment Biophysics, Northwestern Polytechnical University, Xi'an, 710072, China
[d] Department of Vertebra Surgery, Affiliated Longhua People's Hospital, Southern Medical University (Longhua People's Hospital), Shenzhen, 518109, China
[e] Department of Osteoporosis, Honghui Hospital, Xi'an Jiaotong University, Xi'an, 710054, China
[f] Department of Orthopaedics, The Second Affiliated Hospital of Soochow University, Suzhou, 215004, China
[g] Heye Health Technology Co., Ltd, Huzhou, 313300, China

ARTICLE INFO

Keywords:
Bond loss
HAMP deficiency
Iron metabolism
Postmenopausal osteoporosis
Static magnetic field

ABSTRACT

Objective: Clinical studies, epidemiological investigations and animal experiments have demonstrated that iron overload lead to bone loss, especially postmenopausal osteoporosis. As a physiotherapy tool, electromagnetic fields already used in clinical treatment of osteoporosis and participates in bone remodeling by affecting the iron metabolism of organisms. As an electromagnetic field with constant magnetic flux density and direction, the mechanism of static magnetic field (SMF) regulating iron metabolism remains unclear. Therefore, the aim of this study was to investigate the effects of moderate static magnetic field (MMF) on iron metabolism and bone metabolism in postmenopausal osteoporosis and *HAMP*-deficient mouse models, and to elucidate the underlying mechanisms.

Methods: Firstly, the effects of MMF on bone metabolism and iron metabolism in 22 postmenopausal osteoporosis participants were evaluated by comparing the changes of bone mineral density (BMD) and serum ferritin before and after treatment. Secondly, 10-week-old male C57BL/6 $HAMP^{+/+}$ and $HAMP^{-/-}$ mice were randomly divided into four groups, namely GMF-$HAMP^{+/+}$ group and MMF-$HAMP^{+/+}$ group, GMF-$HAMP^{-/-}$ group and MMF-$HAMP^{-/-}$ group (n = 8/group). The MMF-treated mice were exposed daily to MMF, while the remaining group was exposed to geomagnetic field (GMF) for 8 weeks. BMD was scanned and bone tissues were collected for mechanical, structural and histological analysis. In addition, analysis of serum and tissue iron content evaluated the regulation of systemic iron metabolism by MMF. Finally, the effects of MMF on the differentiation of primary macrophages and primary osteoblasts were evaluated *in vitro*.

Results: In clinical trial, MMF decreased serum ferritin levels in postmenopausal osteoporosis patients, which was negatively correlated with changes in lumbar BMD. *In vivo*, the results showed that *HAMP*-deficient mice were accompanied by iron overload, along with reduced lumbar vertebra bone mass and bone quality. MMF improved the bone mass, microstructure and biomechanical properties of lumbar vertebrae in $HAMP^{-/-}$ mice. *In vitro*, MMF reduced the number and differentiation of osteoclasts in $HAMP^{-/-}$ mice, and promoted primary osteoblast differentiation by activating Wnt/β-catenin signaling pathway. Further, MMF also reduced the iron ion conversion and enhanced the antioxidant system of $HAMP^{-/-}$ mice. These data suggested that MMF could regulate iron metabolism and salvage bone loss caused by iron accumulation.

Conclusions: The clinical trial and laboratory results suggested that MMF intervention has a protective effect on bone loss caused by iron metabolism disorders.

Translational potential of this article: Translational potential of this article: This study demonstrated the feasibility and potential effectiveness of MMF in the treatment of postmenopausal osteoporosis patients, demonstrating for

* Corresponding author. Research & Development Institute of Northwestern Polytechnical University in Shenzhen, No. 45, Gaoxin South 9th Road, Nanshan District, Shenzhen, China.
E-mail address: shangpeng@nwpu.edu.cn (P. Shang).

https://doi.org/10.1016/j.jot.2024.10.012
Received 4 June 2024; Received in revised form 13 September 2024; Accepted 31 October 2024
Available online 10 January 2025

the first time that MMF can reduce bone loss in mice with inherited iron metabolism abnormalities. It was suggested that MMF plays an important role in iron metabolism disorders or as an alternative therapy to ameliorate osteoporosis caused by iron accumulation.

1. Introduction

Osteoporosis is a systemic metabolic disease caused by multiple causes, such as aging, menopause or unknown causes, resulting in decreased BMD and bone mass, damage to bone microstructure, and increased bone fragility. It is commonly seen as senile osteoporosis in the elderly after the age of 70 or postmenopausal osteoporosis in women 5–10 years after menopause. In addition, the secondary osteoporosis caused by endocrine diseases or prolonged immobility, such as bed rest and space travel [1]. The common symptom of osteoporosis is spinal deformation. Due to the abundance of trabecular bone, the thoracic and lumbar vertebra of osteoporosis are most prone to compression fracture. In clinical practice, dual-energy X-ray absorptiometry (DEXA) has become the gold standard for diagnosing osteoporosis by detecting the T-scores of the thoracic and lumbar vertebrae [2,3].

Clinical data indicate that whether it is senile osteoporosis, postmenopausal osteoporosis or disuse osteoporosis, iron overload is associated with life. Iron accumulation as an independent risk factor for osteoporosis can lead to bone loss [4,5]. *In vivo*, iron levels in the blood, brain and bone tissue of mice were significantly increased after ovariectomy [6–8]. *In vitro*, cell experiments demonstrated that excess iron induce apoptosis of osteoblasts and osteoclasts, inhibit osteoblast differentiation by down-regulating Wnt/β-catenin signaling pathway and promote osteoclastogenesis by generating a large amount of reactive oxygen species, thus disrupting the balance of bone remodeling [9–11].

Since Bassett reported in the 1970s that electromagnetic fields accelerate fracture healing [12], a large body of evidence has supported the positive efficacy of electromagnetic fields (EMF) as a non-invasive method for skeletal system diseases. In fact, the electromagnetic field includes the time-varying magnetic field and the static magnetic field (SMF), where the SMF is a field with constant magnetic flux density and is independent of time. In the past few decades, studies have found that SMF can prevent osteoporosis, repair bone defects, accelerate fracture healing, and can also assist in the treatment of osteoporosis complications caused by diabetes and ischemia [13–16]. One of the effects of SMF on bone is realized through the regulation of cell differentiation of bone tissue. A large number of studies have proved that SMF can promote the osteogenic differentiation of bone mesenchymal stem cells (BMSCs), improve the mineralization ability of osteoblasts, activating the process of bone formation [17,18]. In addition, SMF can reduce the number of osteoclasts and slow down differentiation, inhibiting bone resorption process. Based on our previous work, we found that iron metabolism is involved in the process of bone reconstruction regulated by SMF [19–21].

The study on the regulation of iron metabolism by EMF started half a century ago [22]. In the past decade, more and more studies have pointed out that the biological effect of SMF is closely related to not only the physical parameters, but also its regulation of iron metabolism. Our team has conducted a comprehensive and in-depth study on the mechanism of SMFs regulating iron metabolism. We found that hypomagnetic field (HyMF, magnetic flux density <5 μT) inhibited the recovery of HLU mice through increasing iron content in the tibia by inhibiting iron excretion [20]. In addition, we found that high static magnetic field (HiSMF, magnetic flux density >1 T) reduces iron content in osteoblast and osteoclast differentiation by inhibiting iron absorption and promoting iron excretion [19,23]. In other words, the regulation of iron metabolism by HiSMF is involved in the differentiation of osteoblasts and osteoclasts. It is not difficult to see that some beneficial effects can be achieved in bone tissue under appropriate exposure to SMF. However, it is unclear whether SMF can still regulate bone remodeling by affecting iron in models of iron metabolism disorders.

To evaluate the therapeutic efficacy and potential mechanisms of MMF (magnetic flux density ranging from 1 mT to 1 T) on postmenopausal osteoporosis and iron metabolism disorders in mouse models, this study examined the effects of MMF exposure on bone quality, structure, and function, as well as the regulation of iron metabolism, in anticipation of the development and application of MMF in the treatment of iron metabolism disorders and their complications.

2. Subjects and methods

2.1. Study participants

This study was performed in accordance with the approved institutional ethical protocol (Ethical Review of Shenzhen Longhua People's Hospital [2021] No.106) and registered at Chinese Clinical Trial Registry (ChiCTR2100048604). The participants underwent health examinations, BMD measurements and serum ferritin tests at Shenzhen Longhua People's Hospital. Participants with T-scores less than −2.5 and without thyroid disease, malignancies, diabetes, abnormal liver and kidney function and other diseases related to bone metabolism. Twenty-two participants aged 50 and above (50–70 years old) were divided into two groups, the control group (n = 11) and the MMF exposure group (n = 11). Participants in the MMF group wore waist belt containing MMF device (Fig. 1) for 6 h per day, five days a week. The control group wore the same material waist belt without MMF for 6 h per day, five days a week. All participants received calcium (1200 mg), calcitriol (50 μg) and salmon calcitonin (50 μg) daily as a basic treatment for osteoporosis. The entire study lasted for 90 days, during which blinding was implemented for participants, clinical examiners, data collectors and data analysts.

2.2. Animals and treatments

Adult *HAMP* heterozygous mice were originally from the Department of Orthopedics at the Second Affiliated Hospital of Soochow University (the targeted destruction of *HAMP* gene can be referred to the previous literature description [24]). Wild-type and knockout offspring were obtained by interbred with *HAMP* heterozygous mice. 10-week-old male C57BL/6 $HAMP^{+/+}$ and $HAMP^{-/-}$ mice were randomly divided into four groups, $HAMP^{+/+}$ mice in GMF and $HAMP^{+/+}$ mice in MMF, $HAMP^{-/-}$ mice in GMF and $HAMP^{-/-}$ mice in MMF (n = 8/group is sufficient). The ambient temperature was set at 24 ± 2 °C, and standard laboratory rodent food and water were freely provided for 8 weeks with 12 h of light and dark cycle per day. The experimental animal program was approved by the Medical and Experimental Animal Ethics Committee of Northwestern Polytechnical University (NO.202301186).

2.3. MMF exposure systems

The MMF used in laboratory was generated by a superconducting magnet (JMTA-16T50MF) (Fig. 1). The magnetic induction intensity is about 0.2 T–0.4 T in the central radial direction of the bottom of the superconducting magnet at 400 mm–500 mm, and the distribution gradient of the magnetic induction intensity is about 2 T/m. Cages made of polymethyl methacrylate and a chamber made of double layers of copper were placed in MMF for feeding mice and cultured cells, respectively. Both the cage and the copper device are 1/4 circular arc with an inner diameter of 400 mm and an outer diameter of 500 mm. The lid of the mouse cage is made of stainless steel, and there is a circulating water bath in the middle of the copper double layer to

achieve temperature control.

2.4. BMD and BMC evaluation

The day before the sacrifice, the mice were anesthetized and scanned for BMD and bone mineral content (BMC) using DEXA (InAlyzer; MEDIKORS, Seongnam, Korea). BMD and BMC of the whole body, femur, tibia and lumbar vertebra were analyzed by using the software (InAlyzer) that matched with the machine.

2.5. Micro-computed tomography analysis

Micro-computed tomography (Micro-CT) equipment (Scanco-VivaCT80; Scanco Medical AG, Switzerland) scanned the fixed bone tissue to visualize the bone microstructure. In simple terms, bone tissue was isolated and fixed in 4 % paraformaldehyde (PFA). The sample was fixed on the sample holder and scanned with a Micro-CT device with an isotropic resolution of 10.4 μm (Energy: 70 kV, 114 μA; exposure time: 205 ms per frame), using built-in software to capture images. All data was analyzed by SCANCO Appication Evaluation Software, and 3D reconstruction is performed by Ray Tracer software. The main parameters of trabecular bone include bone volume fraction (BV/TV), trabecular number (Tb.N), trabecular separation (Tb.Sp) and connectivity density (Conn.D). The main parameters of cortical bone include cortical thickness (Ct.Th), cortical porosity (Ct.Po), pore number (Po.N) and total volume of pore space (Po.V).

2.6. Mechanical properties testing

The mechanical properties of bone were evaluated by universal material testing machine (Instron 5943; Instrong, MA). Lumbar vertebra and tibia remove soft tissue spinous process and articular process. The KH-8700 digital microscope (HIROX, Japan) was used to measure the length diameter, short diameter and height of the vertebra. Then, the bone tissue was placed on the bottom platform of the testing machine, and the cylinder head was loaded at a speed of 1 mm/min until it was deformed. Compression tests were performed on the lumbar vertebra and three-point bending tests were performed on the tibia. The KH-8700 digital microscope was used to measure the inside and outside diameters of the tibia fracture surface. The load–displacement curve and stress–-strain curve were recorded, and the parameters including ultimate load, stiffness, modulus and toughness were calculated.

2.7. Histological and analysis

The lumbar vertebra and femur were decalcified in 10 % EDTA (replaced with fresh solution every 3 days) for 2 weeks, followed by paraffin embedding. H&E and TRAP staining were performed on sections with a thickness of 5 μm using a semi-automatic rotary microtome (Science; China) to examine the osteoblast number per bone surface (N.Ob/BS), the osteoclast number per bone surface (N.Oc/BS) and osteoclast surface per bone surface (Oc.S/BS).

2.8. Iron content measurements

The heart, liver, spleen, kidney, pancreas, skull, lumbar vertebra and tibia were dried at 120 °C for 4 h and then weighed. After ashing at 600 °C, these tissues were dissolved at 70 °C in concentrated nitric acid. The samples were diluted with ultra-pure water and the iron content was determined by atomic absorption spectrometry (AAS; Analytik Jena AG; Jena, Germany). The ratio of iron content to tissue weight was normalized. To observe iron deposition in heart, liver, spleen, kidney, pancreas, skull, lumbar vertebra and tibia, the tissue samples were embedded with paraffin wax and sliced 5 μm. The Prussian blue stain was enhanced with diaminobenzidine (DAB).

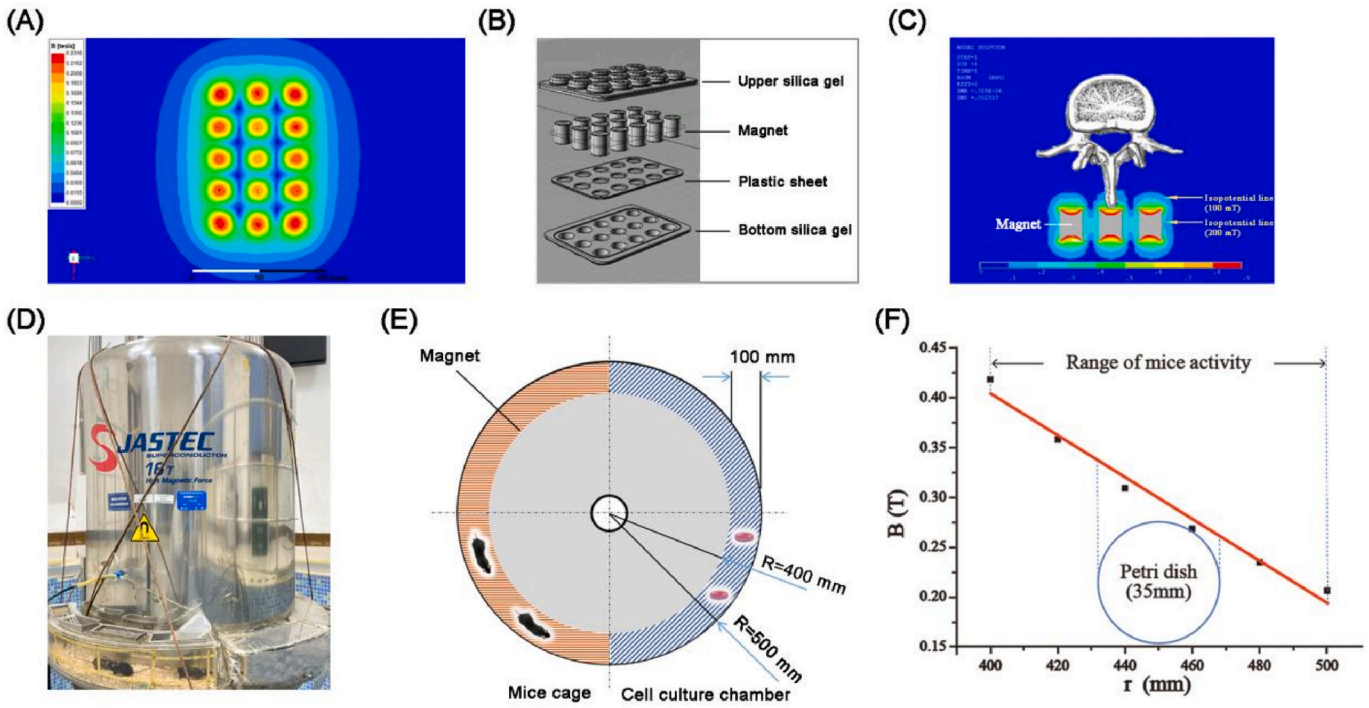

Fig. 1. Moderate static magnetic field (MMF) devices for clinical trials and laboratory studies. (A) Schematic diagram of magnetic induction intensity distribution of MMF magnets, (B) structure of magnet modules and (C) simulation of magnetic field distribution of the vertebrae exposed in MMF using ANSYS for clinical trials. (D) JMTA-16T50MF superconducting magnet and MMF at the bottom of the magnet, (E)–(F) top view of mice activity or cell culture location in the MMF, and magnetic induction intensity in this range.

2.9. Serum biochemical analysis

The contents of serum ferritin, P1NP and βCTx-1 were determined by enzyme-linked immunosorbent assay (ELISA). All steps follow the manufacturer's instructions. ELISA kit of ferritin (JL20638), P1NP (JL20174) and βCTx-1 (JL31101) were purchased from Jianglai Biotechnology Company.

2.10. Immunohistochemistry

The duodenum was collected and placed in 4 % PFA overnight. The tissue samples were embedded with paraffin wax and sliced 5 μm. During immunohistochemical staining, duodenal slides underwent dewaxing, hydration, thermal antigen repair, and then incubated with FPN (Affinity, #DF13561) antibody at 4 °C overnight. On the second day, the slides were washed with PBS and incubated with secondary antibody at room temperature for 1 h.

2.11. Primary bone marrow-derived macrophages culture

Primary bone marrow-derived macrophages (BMMs) were prepared as reported previously. Murine bone marrow cells were obtained by flushing the tibias and then cultured in complete α-Minimum Essential Medium (α-MEM) (Invitrogen, Carlsbad, CA, USA) containing 30 % L929 cell medium supernatant with 10 % fetal bovine serum (FBS). The adherent cells after 3 days of culture were used as BMMs.

2.12. Primary skull -derived osteoblasts culture

Primary osteoblasts were isolated from the skull by collagenase after anesthesia in neonatal mice 3–5 days old. The primary osteoblasts were cultured in α-MEM containing 10 % FBS. The adherent cells cultured for 7 days were used as primary osteoblasts. On the basis of normal medium, 50 μg/mL ascorbic acid and 10 mM β-glycerophosphate disodium salt hydrate were added for osteogenic differentiation, and fresh medium was replaced in the petri dish every 2 days.

2.13. Mineralization assay

Primary osteoblasts were differentiated for 14 days, and the cells were fixed in 4 % PFA and stained by 0.1 % Alizarin red S (Sigma–Aldrich). Positive alizarin red staining for calcified nodules represents osteoblast mineralization. Alizarin red stained osteoblasts were photographed by a scanner, and the ratio of the area of calcified nodules to the area of the bottom of the petri dish was measured by Image J software.

2.14. Alkaline phosphatase assay

After 7 days of primary osteoblast differentiation, the cells were washed once with 0.01M phosphate buffer solution (1 × PBS) and then fixed in 4 % PFA for 20 min. A BCIP/NBT alkaline phosphatase (ALP) color development kit (Beyotime, C3206) was used to stain ALP, and the ratio of the area of ALP to the area of the bottom of the petri dish was measured by Image J software.

2.15. TRAP staining

Primary BMMs were induced to differentiate in α-MEM containing 50 ng/mL RANKL for 9 days. The cells were then fixed with 4 % PFA and stained with an acid phosphatase kit (Sigma–Aldrich, CS0740) according to the manufacturer's instructions. Dark red cells containing three or more nuclei are considered TRAP-positive multinucleated cells.

2.16. F-actin ring immunofluorescence staining

Primary BMMs were induced to differentiate in α-MEM containing 50 ng/mL RANKL for 9 days. Then it was fixed with 4 % PFA, permeated with 0.1 % TritonX-100 and 1 % BSA buffer, and the Actin Tracker Red-555 (Beyotime, C2203S) was diluted into PBS buffer at a ratio of 1:200. On the second day, DAPI dye solution was diluted with PBS in a ratio of 1:500 for nuclear staining. Finally, it was washed with PBS buffer 3 times, observed and imaged under inverted fluorescence microscope (ZEISS, Observer 3).

2.17. Osteoclast resorption assay

Primary BMMs were induced to differentiate in α-MEM containing 50 ng/mL RANKL for 24 days. After the experiment, the medium was discarded and 200 μL sodium hypochlorite was added for incubation at room temperature for 10 min. Then, the wells were rinsed with deionized water and photographed with inverted microscope (ZEISS, Observer 3). The osteoclast absorption activity was measured by Image J software, and expressed as the ratio of pits area to the total photo area and the number of pits per unit area.

2.18. Measurement of MDA

After tissue or cell lysis, supernatant was obtained by centrifugation at a speed of 12,000 g, and the working liquid was detected by MDA kit (Beyotime, S0131S). After heating at 100 °C for 15 min, OD value at 532 nm was detected by multifunctional enzyme marker (BIO-TEK, Synergy HT). The MDA content is calculated according to the standard curve, and the MDA content in the initial sample is expressed by the protein content per unit weight (nmol/mg protein).

2.19. Measurement of GSH/GSSG

Tissues and cells were added with protein removal reagent solution and suspended, and the samples were freeze-thawed twice with liquid nitrogen and 37 °C water bath, supernatant liquid was taken to determine glutathione, and the GSH scavenging assistant solution and glutathione detection working solution were added in proportion. After incubation at 37 °C for 5 min, OD value at 412 nm was detected with a multifunctional enzyme marker (BIO-TEK, Synergy HT). The reduced GSH content was obtained by subtracting the GSSG content from the total glutathione content. The GSH level was normalized according to the protein concentration, and the ratio of reduced GSH/GSSG was calculated.

2.20. Measurement of ROS

Primary BMMs were induced to differentiate in α-MEM containing 50 ng/mL RANKL for 9 days. DCFH-DA (Solarbio, CA1410) probe was loaded in situ, diluted with serum-free medium at 1:1000 ratio, the final concentration was10 μM, and incubated at 37 °C for 20 min. The cells were washed 3 times with serum-free medium. Hoechst33342 (Beyotime, C1028) was diluted with serum-free medium at 1:500 ratio to restain nuclei and incubated at 37 °C for 5 min. After incubation, serum-free medium was washed 3 times and photographed with inverted fluorescence microscope (ZEISS, Observer 3).

2.21. Immunofluorescence assay

Primary BMMs were induced to differentiate in α-MEM containing 50 ng/mL RANKL for 9 days. After the cells were fixed, permeated and sealed, Keap1 antibody (Affinity, AF5266) was diluted at a ratio of 1:200 and incubated at 4 °C overnight. The next day, the FITC-labeled secondary antibody (Servicebio, GB22303) was incubated at room temperature in a shaker for 2 h. After incubation, PBS was washed 3 times, photographed with inverted fluorescence microscope (ZEISS, Observer 3).

2.22. Western blot

The lumbar vertebra, duodenum and cells were lysed and supernatant was obtained by centrifugation. Protein in supernatant samples was quantified and separated by sodium dodecyl sulfate polyacrylamide gel electrophoresis (SDS-PAGE). The protein is then transferred to a polyvinylidene fluoride (PVDF) membrane. The membrane was blocked with 5 % skim milk at room temperature for 3 h and incubated with the following antibodies: runt-related transcription factor 2 (Runx2, CST, #12556), collagen type I (COL-1, Proteintech, 14695-1-AP), osteocalcin (OCN, Abclonal, A6205), alkaline phosphatase (ALP, Abcam, ab133602), osteopontin (OPN, Proteintech, 22952-1-AP), Wnt5a (Abcam, ab227229), low-density lipoprotein receptor protein 6 (LRP6, Abclonal, A22661), dishevelled segment polarity protein 2 (DVL2, CST, #3224), β-catenin (Proteintech, 51067-2-AP), nuclear factor kappa-B (NF-κB p65, Affinity, AF2006), nuclear factor of activated T cells 2 (NFATc2, CST, #8032), matrix metalloproteinase-9 (MMP9, Proteintech, 10375-2-AP), cathepsin K (CTSK, Proteintech, 11239-1-AP), transferrin receptor protein 1 (TfR1, Abclonal, A21622), six-transmembrane epithelial antigen of the prostate 3 (steap3, Abclonal, A0683), divalent metal transporter 1 (DMT1, Proteintech, 20507-1-AP), ferritin heavy chain 1 (FTH1, Abcam, ab183781) and ferroptin (FPN, Proteintech, 26601-1-AP), nuclear factor erythroid 2 related afctor 2 (Nrf2, Abcam, ab62352) , superoxide dismutase1 (SOD1, Abcam, ab308181). After washing with Tween-20 solution (TBST), it was incubated with horseradish peroxidase coupled secondary antibody. Each band was visualized by enhanced chemiluminescence (ECL) colorimetry, and the image was captured by chemiluminescence system (T5200Multi; Shanghai Peiqing Technology Co., Ltd., Shanghai, China).

2.23. Quantitative real time PCR analysis

Total RNA was extracted by using HiPure Total RNA Mini Kit (Magen, Guangzhou, China). RNA reverse transcription was performed using HiScript II Q RT SuperMix (Vazyme, Nanjing, China) followed by quantitative real-time PCR using specific primers. The expression of the target gene was normalized to the respective GAPDH levels. The primer sequences are shown:

GAPDH: Forward primer: (TGCACCACCAACTGCTTAG), Reverse primer: (GGATGCAGGGATGATGTTC);

RANKL: Forward primer: (GTACTTTCGAGCGCAGATGGA), Reverse primer: (GCAGGAGTCAGGTAGTGTGTC);

NFATc1: Forward primer: (CCAGCTTTCCAGTCCCTTCC), Reverse primer: (ACTGTAGTGTTCTTCCTCGGC);

NF-κB: Forward primer: (TCCGCTATGTGTGTGAAGGC), Reverse primer: (TGCAAATTTTGACCTGTGGGT).

2.24. Statistical analysis

Statistical analysis was performed using GraphPad Prism 8 software (version 8; GraphPad Software, Inc., La Jolla, CA, USA). The data were displayed in mean ± standard deviation (SD). Mean percentage change data are expressed as mean ± standard error (SE), showing both median and quartile rangeand. The significance of differences among experimental groups was determined by *t-test*, one-way ANOVA with Tukey's multiple comparisons test or two-way ANOVA with Sidak's multiple comparisons test. The value of $P < 0.05$ was considered statistically significant.

3. Results

3.1. MMF decreased serum ferritin levels in postmenopausal osteoporosis, which was negatively correlated with lumbar BMD

It has been proved that serum iron overload in postmenopausal osteoporosis patients, and iron accumulation is a negative regulator of bone metabolism. However, it remains unclear that the effects of SMFs on serum ferritin and BMD in postmenopausal osteoporosis patients. To explore this question, we collected data from 22 postmenopausal women who were treated with or without MMF for 90 days, and evaluated measures of serum ferritin and lumbar BMD. Comparing the two groups, it was found that the increase of T-score in MMF treatment group (+5.91 % ± 2.82 %) was higher than that in control group (+2.47 % ± 2.38 %) (Fig. 2A). Compared with control group (+1.80 % ± 5.71 %), MMF treatment reduced serum ferritin (−11.69 % ± 4.51 %) by approximately 13.49 % (Fig. 2B and C). Linear correlation analysis showed that there was a negative correlation between the rate of serum ferritin change and the rate of lumbar BMD change (Pearson $r = -0.6088$, $P = 0.0468$) (Fig. 2D). These results suggested that MMF could reduce serum ferritin in postmenopausal women and which was negatively correlated with lumbar BMD.

3.2. Duodenal iron absorption increased and iron distribution in vivo altered in $HAMP^{-/-}$ mice

Hepcidin is a core member that regulates iron metabolism in the body, so the basic situation of iron metabolism in $HAMP^{-/-}$ mice were examined first. After *HAMP* knockout, FPN expression was increased in duodenal villous epithelial cells (Fig. 3A). FPN is the only iron transporter found in mammals, and this result indicates that $HAMP^{-/-}$ mice absorb more iron from diet than $HAMP^{+/+}$ mice. The heart, liver, kidney, pancreas, skull, lumbar trabeculae and femoral trabeculae of $HAMP^{-/-}$ mice showed ignificant hemosiderin deposits, while the spleen was the opposite (Fig. 3F–H), and the fresh liver and pancreatic tissues showed distinct rust red (Fig. 3B and C). $HAMP^{-/-}$ mice had increased serum iron and ferritin levels compared to wild-type mice (Fig. 3D and E).

3.3. MMF improved bone mass and microstructure in $HAMP^{-/-}$ mice

Osteoporosis is a systemic metabolic disease in which fragility fractures increase due to the pathological decline of bone mass and the destruction of bone microstructure. Compared with $HAMP^{+/+}$ mice, BMD and BMC did not fluctuate in the femur and tibia of $HAMP^{-/-}$ mice, but decreased in the lumbar vertebra. However, BMD and BMC increased in the lumbar vertebra and tibia of $HAMP^{-/-}$ mice after exposure to MMF, while wild-type mice did not visible difference (Fig. 4A and B). At the same time, it can be seen from Fig. 4C and D that the lumbar vertebra of $HAMP^{-/-}$ mice showed lower BV/TV, Tb.N and Conn.D, but higher Tb.SP. After exposure to MMF, the micro-structural parameters of lumbar vertebra in $HAMP^{-/-}$ mice were improved, including increased BV/TV and decreased Tb.SP, while $HAMP^{+/+}$ mice did not significantly change these parameters. In the long bones of $HAMP^{-/-}$ mice, cortical bone had higher Ct.Po, Po.N, Po.V, and trabecular bone had less Tb.N and higher Tb.SP. After exposure to MMF, the Ct.Po, Po.N and Po.V of cortical bone decreased, but there were no significant difference between Tb.N and Tb.SP of trabecular bone (Figs. S1A–D).

3.4. MMF improved bone biomechanical properties in $HAMP^{+/+}$ and $HAMP^{-/-}$ mice

The deterioration of bone micro-structure implies a weakening of bone's ability to withstand mechanical property. The lumbar vertebra exhibited poor mechanical load bearing capacity, as demonstrated by reduced ultimate load, stiffness and compression modulus in $HAMP^{-/-}$ mice (Fig. 5A–C). However, the mechanical properties of the tibia in $HAMP^{-/-}$ mice showed a decreasing trend without statistical difference (Figs. S1E–H). After 8 weeks of MMF exposure, ultimate load, stiffness, compression modulus and ultimate stress of lumbar vertebra were improved to varying degrees in both $HAMP^{+/+}$ mice and $HAMP^{-/-}$ mice (Fig. 5A–D). At the same time, the elastic modulus and ultimate stress of

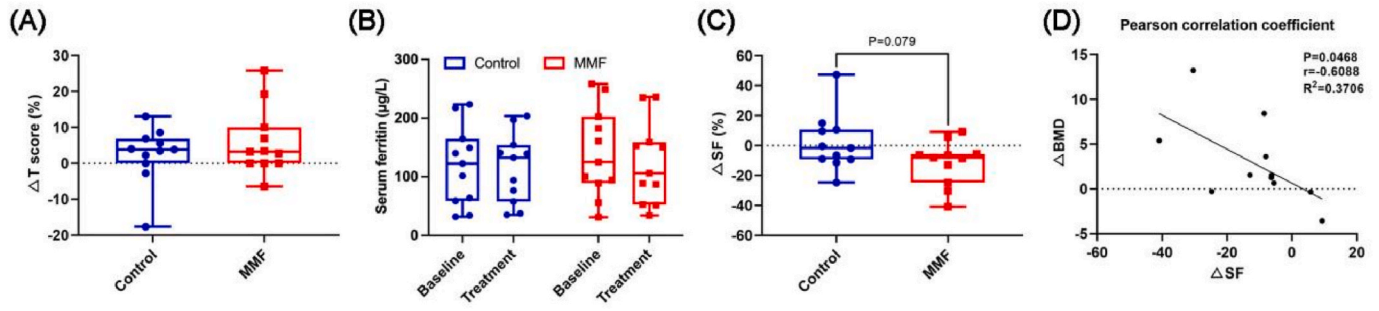

Fig. 2. Effect of MMF on iron metabolism and bone metabolism in postmenopausal osteoporosis participants. (A) Change rate of lumbar T-score after MMF treatment. (B) Participants' serum ferritin levels before/after MMF treatment. (C) The change rate of serum ferritin after MMF treatment. (D) Correlation analysis between serum ferritin change rate and lumbar BMD change rate. Each point in the bar represents an individual participants with n = 11/group.

the tibia in *HAMP*$^{-/-}$ mice were improved (Figs. S1G and H). These results suggested that MMF promote the mechanical bearing capacity of the lumbar vertebra in normal mice, and improved the lumbar vertebra biomechanical properties of *HAMP*$^{-/-}$ mice to normal mice level.

3.5. MMF inhibited bone resorption in HAMP$^{+/+}$ and HAMP$^{-/-}$ mice

Osteoclasts mediate the bone resorption process and are characterized by the secretion of TRAP. TRAP staining was performed on the lumbar vertebra and femur to examine trabecular bone resorption. In lumbar tissue, the number and area of TRAP positives in *HAMP*$^{-/-}$ mice were significantly higher than those in *HAMP*$^{+/+}$ mice, via N.Oc/BS and Oc.S/BS revealed, and MMF exposure inhibited lumbar bone resorption in *HAMP*$^{+/+}$ mice and *HAMP*$^{-/-}$ mice (Fig. 6A and B). In the femur tissue of *HAMP*$^{-/-}$ mice, the characteristics of TRAP-positive cells showed the same trend as in the lumbar vertebra, but the difference was not as significant as in the latter (Figs. S2A and B). The content of bone turnover marker β-CTx in serum of *HAMP*$^{-/-}$ mice was higher than that of wild-type controls, and MMF reversed this phenomenon (Fig. 6C). At the cellular level, primary BMMs isolated from *HAMP*$^{-/-}$ mice showed more TRAP positivity during differentiation into multinuclear giant cells than *HAMP*$^{+/+}$ murine-derived cells, and MMF exposure inhibited TRAP activity in murine-derived primary cells with both genes (Fig. 6D). Similarly, primary BMMs isolated from *HAMP*$^{-/-}$ mice formed more and larger F-actin rings than that from *HAMP*$^{+/+}$ mice, and MMF exposure decelerated this process (Fig. 6E). Coincidentally, it showed the same trend of bone resorption function (Fig. 6F).

3.6. MMF inhibited excessive bone resorption activity in HAMP$^{-/-}$ mice by inactivating NF-κB

Primary BMMs were isolated from *HAMP*$^{+/+}$ and *HAMP*$^{-/-}$ mice to detect protein expression during osteoclast differentiation *in vitro*. Results showed that the expression of NF-κB, NFATc2 and CTSK in mononuclear macrophages isolated from *HAMP*$^{-/-}$ mice was higher than that of *HAMP*$^{+/+}$ mice. Exposure to MMF significantly decreased the expression of NFATc2, MMP9 and CTSK (Fig. 7A and B). Similarly, this trend was confirmed in the mRNA expression of the lumbar vertebra in mice (Fig. 7C).

3.7. MMF promoted differentiation of HAMP$^{+/+}$ and HAMP$^{-/-}$ derived primary osteoblasts through Wnt/β-catenin signaling pathway

Trabecular bone formation of lumbar vertebra was examined by classical H&E staining. In lumbar tissue, MMF exposure did not change N.Ob/BS in *HAMP*$^{-/-}$ mice, the bone turnover marker P1NP in serum of mice did not visible difference (Figs. S3A–D).

At the cellular level, there was no difference in the differentiation ability of primary osteoblasts isolated from *HAMP*$^{+/+}$ mice and *HAMP*$^{-/-}$ mice. MMF exposure promoted the differentiation capacity of both *HAMP*$^{+/+}$ and *HAMP*$^{-/-}$ derived primary osteoblasts, as shown by ALP staining and mineralized nodular formation (Figs. S3E and F). Expressions of Runx2, COL-1, OCN, ALP and OPN in primary osteoblasts derived from *HAMP*$^{-/-}$ were lower than those derived from *HAMP*$^{+/+}$, while MMF exposure increased the expression of characteristic proteins during differentiation of primary osteoblasts. We tracked the expression of cascaded molecules associated with Wnt/β-catenin signaling pathway, and found that Wnt5a, LRP6, DVL2 and β-catenin, were all reduced in primary osteoblasts derived from *HAMP*$^{-/-}$. MMF upregulated the relative expression of Wnt5a, LRP6 and β-catenin in primary osteoblasts, whether *HAMP*$^{+/+}$ derived or *HAMP*$^{-/-}$ derived (Figs. S3G and H).

3.8. MMF regulated iron metabolism in HAMP$^{+/+}$ and HAMP$^{-/-}$ mice

The changes of iron metabolism in mice were examined. First, after *HAMP* knockout, duodenal receptor protein FPN expression was increased, while MMF had no significant effect on its expression. It is because of FPN overexpression that *HAMP*$^{-/-}$ mouse duodenal epithelial cells have almost no iron deposition (Fig. 8A and B). Next, iron content and ferritin in serum, as well as iron content in tissues were measured. Compared with *HAMP*$^{+/+}$, the serum and liver iron content of *HAMP*$^{-/-}$ mice was increased, and MMF again increased the iron content in *HAMP*$^{-/-}$ mice, without affecting the iron content of wild-type mice. Prussian blue staining of tissue sections confirmed these trends (Fig. 8C, D, E). After *HAMP* knockout, iron content in spleen of mice was significantly reduced, which was also reflected in the results of tissue iron detection and Prussian blue staining. Finally, we focused on iron metabolism in the lumbar vertebra of mice. According to the Prussian blue stained sections of the lumbar vertebra, iron in *HAMP*$^{+/+}$ mice was mainly distributed in the bone marrow, while iron was mainly deposited on the trabecular surface of bone in *HAMP*$^{-/-}$ mice (Fig. 8D). The results were consistent with those of iron content in lumbar bone matrix measured by atomic absorption meter (Fig. 8E). MMF decreased *HAMP*$^{+/+}$ mice but increased *HAMP*$^{-/-}$ mice lumbar vertebra iron. Next, the expression of important proteins in iron metabolism was examined. Naturally, FPN in the lumbar vertebra of *HAMP*$^{-/-}$ mice was highly expressed. In *HAMP*$^{-/-}$ models with known high iron content, the expression of TfRc, DMT1 and steap3 was significantly higher than in the wild-type group. After 8 weeks of MMF exposure, *HAMP*$^{+/+}$ mice showed decreased expression of DMT1 and FPN in lumbar vertebra, and *HAMP*$^{-/-}$ mice showed decreased expression of steap3, DMT1 and FPN (Fig. 9A).

Since iron can participate in the Fenton reaction to produce hydroxyl radicals, the REDOX state and iron metabolism is closely related. The results showed that a large amount of iron entered and exited from the lumbar vertebra of *HAMP*$^{-/-}$ mice, but MMF reduced iron conversion in the tissue by inhibiting the expression of steap3 and DMT1 (Fig. 9A, Fig. S4A). Although MMF did not reduce MDA levels in lumbar vertebra of *HAMP*$^{-/-}$ mice (Fig. 9B), MMF increased the GSH/GSSH ratio in the

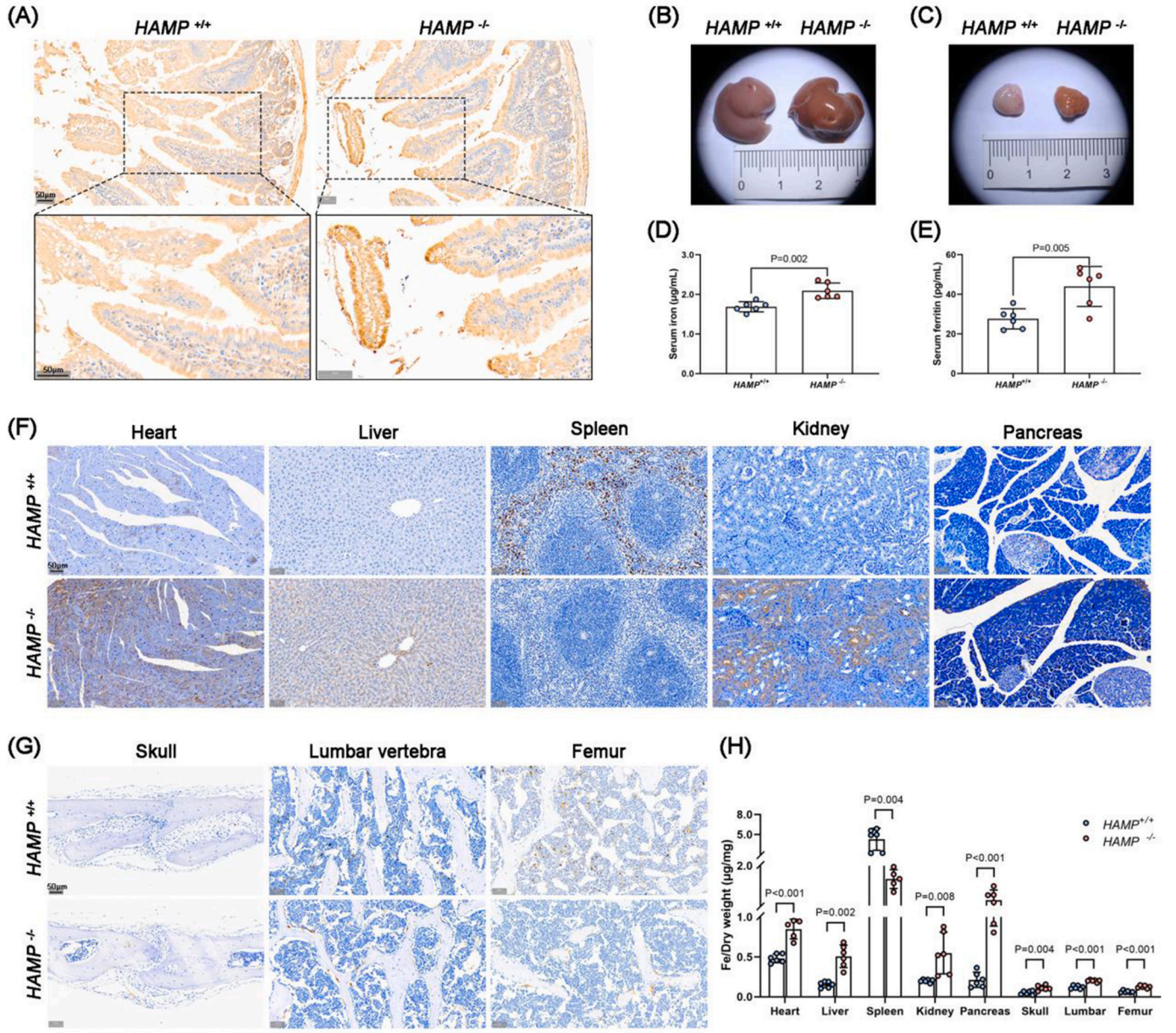

Fig. 3. Comparison of iron metabolism in $HAMP^{+/+}$ and $HAMP^{-/-}$ mice. (A) The expression of FPN in duodenum of $HAMP^{+/+}$ and $HAMP^{-/-}$ mice was detected by immunohistochemistry (Scale bar = 50 μm). (B)–(C) Liver and pancreas tissues in $HAMP^{+/+}$ and $HAMP^{-/-}$ mice at 18 weeks of age. (D)–(E) The serum iron content was determined by atomic absorption spectrometry (AAS) and the serum ferritin concentration was detected by SF ELISA kit. (F)–(G) Iron deposits in heart, liver, spleen, kidney, pancreas, skull, lumbar vertebra and femur of mice were stained with Prussian blue followed incubation with diaminobenzidine (DAB) (Scale bar = 50 μm) and (H) iron contents in tissues were measured by AAS. Each point in the bar represents an individual animal with n = 5–6/group. (For interpretation of the references to color in this figure legend, the reader is referred to the Web version of this article.)

antioxidant system (Fig. 9C). Although iron intake was reduced in primary BMMs of $HAMP^{-/-}$ mice after exposure to MMF, iron conversion in cells was frequent and ROS in cells were active (Fig. 9D and G, Fig. S4B). Keap1/Nrf2 signaling pathway is one of the important mechanisms of cellular defense against oxidative stress damage. Immunofluorescence imaging showed that Keap1 remained quiescent in osteoclasts, where it was activated and separated from the effector after exposure to MMF (Fig. 9H). Protein expression detection showed that the Keap1 binding Nrf2 was isolated after osteoclasts were exposed to MMF, which activated the downstream SOD1 expression (Fig. 9E and F). In conclusion, MMF regulated iron content in bone tissue and enhanced the antioxidant system in response to iron status.

4. Discussion

Hepcidin is a key regulator of systemic iron homeostasis secreted by the liver, and FPN, as the only known iron efflux protein in mammals, is the target of the former. When combined with hepcidin, FPN ubiquitination degrades and loses the function of effecting iron ions. Once the expression of *HAMP* is inhibited, the dysfunction of FPN leads to the abnormal function of iron efflux, which will lead to the disorder of iron metabolism in the body [25]. Duodenal epithelial cells and macrophages were the most abundant sites of FPN expression [26]. In *HAMP* deletion models, iron deposition in these two tissues is reduced due to FPN overexpression, forced iron uptake by duodenum and massive iron output by macrophages, while iron deposition in other tissues such as heart, liver, pancreas and bone is significantly increased. In the iron

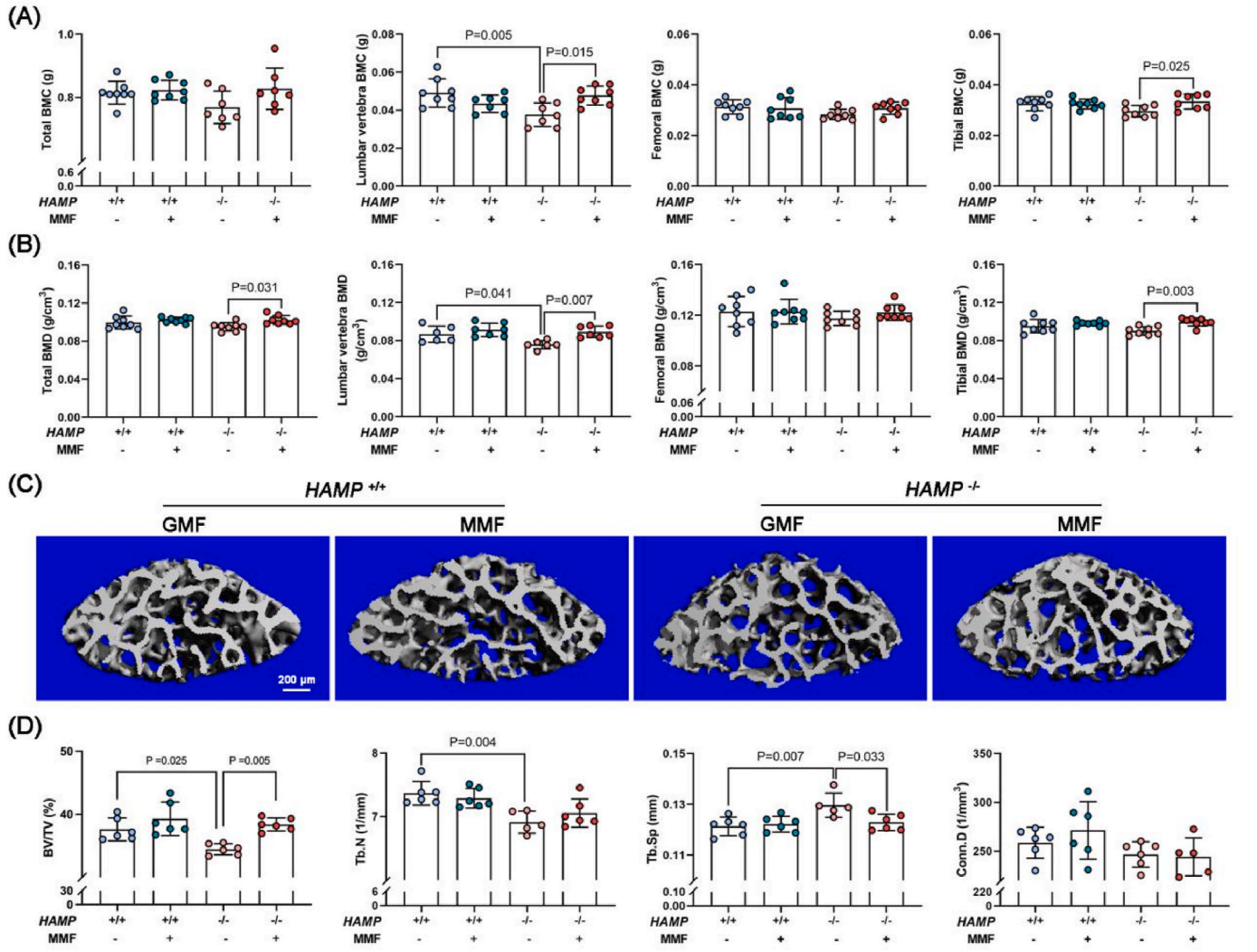

Fig. 4. Effects of MMF on bone mass and micro-structure of bone tissues in $HAMP^{+/+}$ and $HAMP^{-/-}$ mice. (A) BMC, (B) BMD of total, lumbar vertebra, femur and tibia measured by DEXA. (C) Three-dimensional image of trabecular bone structure of lumbar vertebra (Scale bar = 200 μm). (D) Structural parameters of trabecular bone, including BV/TV (%), Tb.N (1/mm), Tb.Sp (mm), Conn.D (1/mm^3). Each point in the bar represents an individual animal with n = 6–8/group.

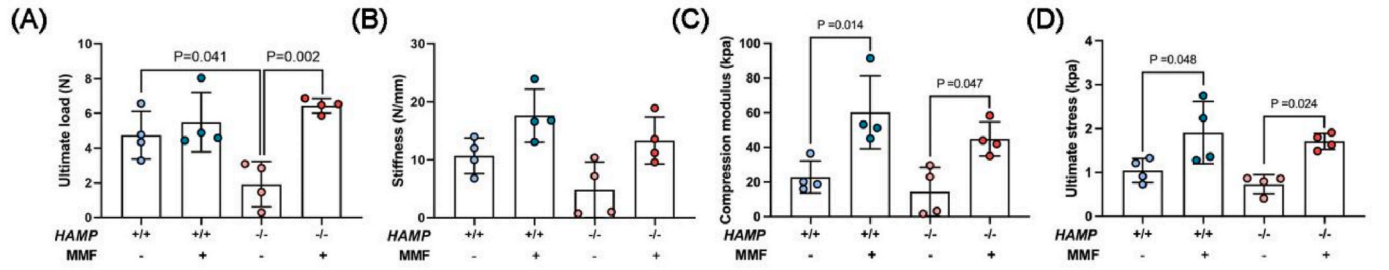

Fig. 5. Effects of MMF on lumbar vertebra biomechanical properties in $HAMP^{+/+}$ and $HAMP^{-/-}$ mice. (A) Ultimate load (N), (B) stiffness (N/mm), (C) compression modulus (kPa), (D) ultimate stress (kPa) of lumbar vertebra. Each point in the bar represents an individual animal with n = 4/group.

metabolism disorder model, iron accumulation is a chronic and long-term process. Female and male *HAMP*-deletion models were compared, and the bone health of male mice was continuously threatened as they aged due to a lack of estrogen (Figs. S5A and B). Specifically, 18-week-old male $HAMP^{-/-}$ mice had reduced bone mass in lumbar vertebra and long bones, deteriorated bone microstructure, and impaired bone strength. In this study, we investigated for the first time the effects of MMF on bone mass, structure and property in mice with abnormal iron metabolism. After 8 weeks of MMF exposure, bone mass in the lumbar vertebra of $HAMP^{-/-}$ mice was increased, and the number and arrangement of bone trabecular were improved, which together led to significant improvements in the biomechanical property of the lumbar vertebra, such as ultimate load, stiffness, compression modulus and toughness.

The imbalance of bone remodeling in $HAMP^{-/-}$ mice was more obviously reflected in increased bone resorption activity *in vivo* and *in vitro*, such as a sudden increase in serum β-CTx, the increase of osteoclasts in bone tissue, and the enhancement of differentiation of primary

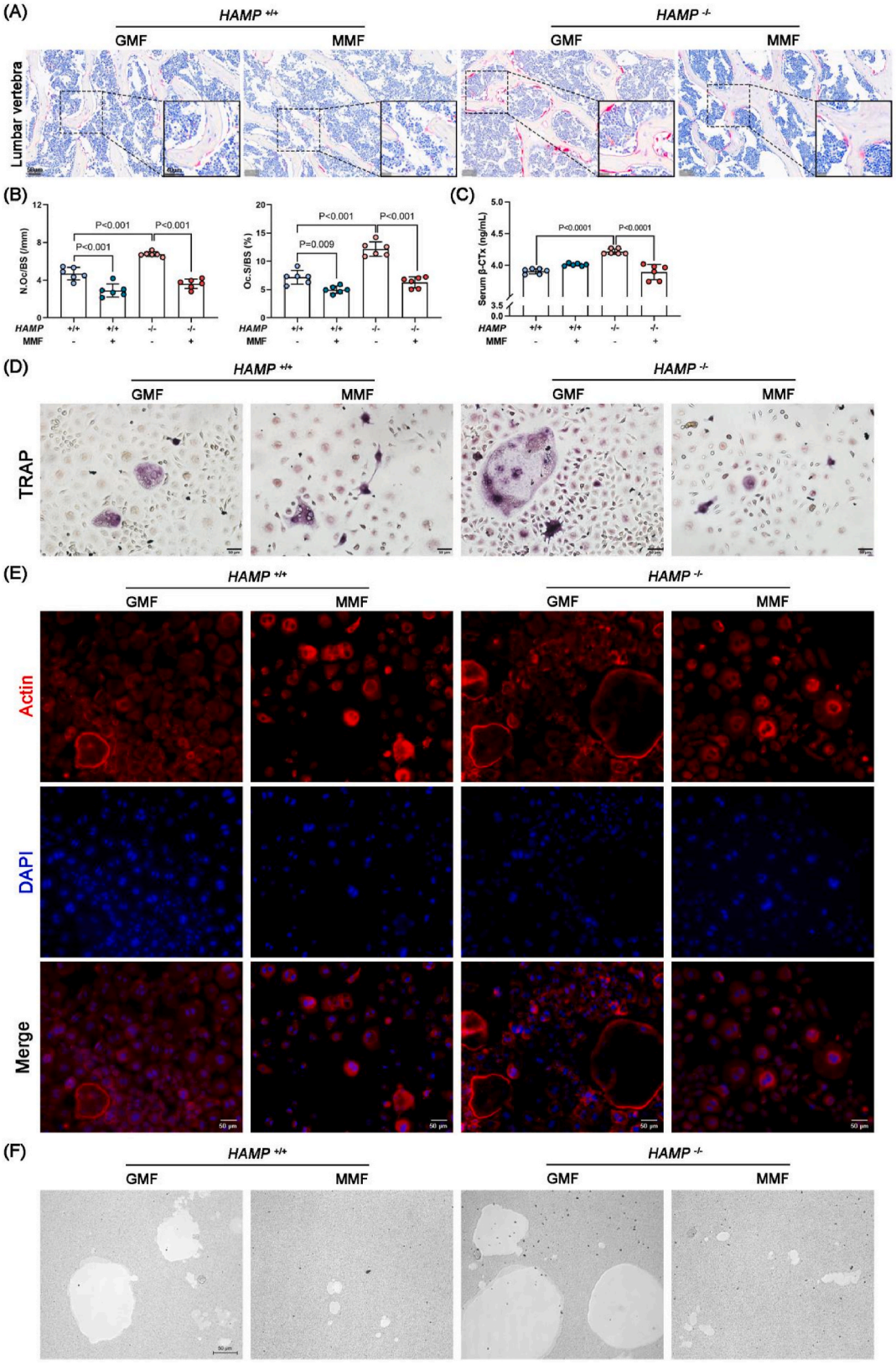

Fig. 6. Effects of MMF on bone resorption in $HAMP^{+/+}$ and $HAMP^{-/-}$ mice. (A) Representative image of stained by TRAP in the trabecular bone of the lumbar vertebra (Scale bar = 50 μm). (B) The number of osteoclasts was estimated by N.Oc/BS (1/mm) and the surface of osteoclasts was estimated by Oc.S/BS (%) of lumbar vertebra. (C) Serum bone turnover marker of βCTx-1. (D) TRAP staining of osteoclasts and (E) F-Actin rings of osteoclasts were detected by Alexa Fluor 555 labeled phalloidin staining and nuclei were detected by DAPI (Scale bar = 50 μm). (F) Representative image of the resorption pits of osteoclasts (Scale bar = 50 μm). Each point in the bar represents an individual animal or petri dish with n = 6/group.

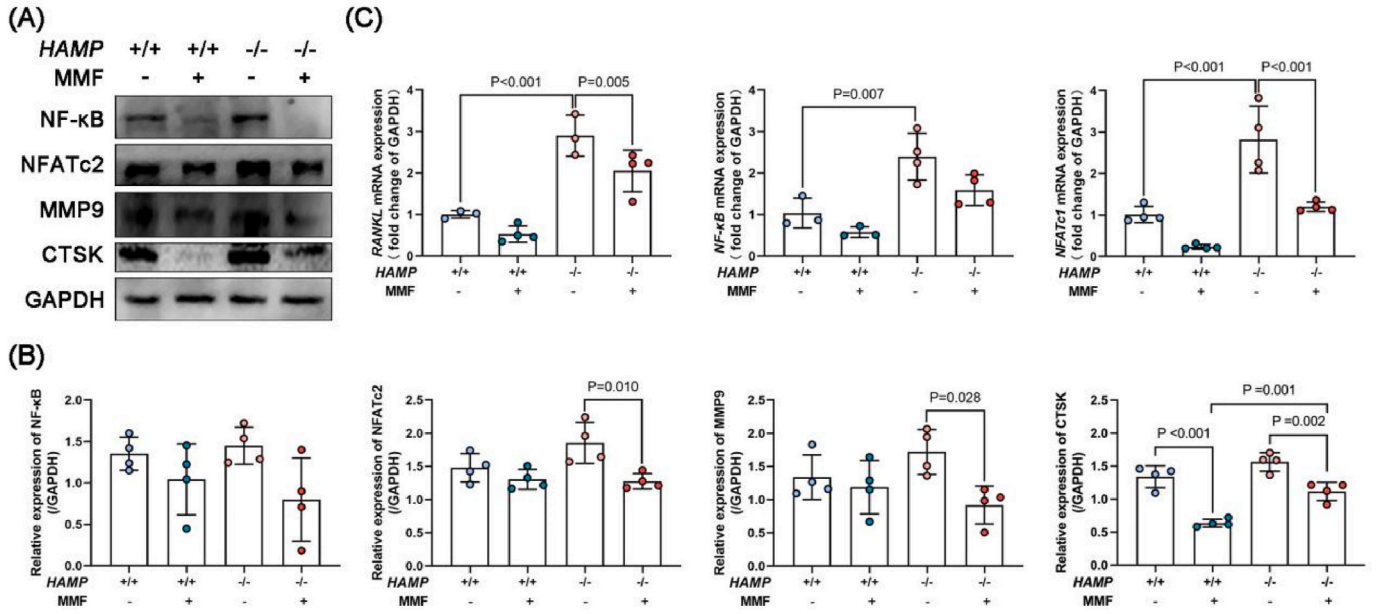

Fig. 7. Effects of MMF on expression of bone resorption-related protein in $HAMP^{+/+}$ and $HAMP^{-/-}$ mice. (A) Protein expression level of NF-κB, NFATc2, MMP9 and CTSK in primary mononuclear macrophages, (B) quantitative analysis of expression levels of NF-κB, NFATc2, MMP9 and CTSK based on western blot. (C) mRNA expression of RANKL, NF-κB and NFATc1 in lumbar vertebra was detected by qPCR. Each point in the bar represents an individual petri dish with n = 3–4/group.

mononuclear macrophages into osteoclasts. However, there have been other reports that after *HAMP* gene deletion, the bone formation process is inhibited and the bone resorption process is not changed, leading to bone mass reduction, which seems to have reached a contradictory conclusion [27,28]. In fact, the age of the subjects was a key influencing factor. As the mice aged, bone formation was less efficient in older mice, while bone resorption was about the same as in younger mice [29]. As a result, iron overload has no obvious effect on bone resorption but significantly inhibits bone formation in old mice. In this experiment, exposure to MMF for 8 weeks significantly alleviated bone resorption activity in 18-week-old mice, especially in $HAMP^{-/-}$ mice. Although there were no significant differences between wild-type mice and $HAMP^{-/-}$ murine-derived osteoblasts, MMF promoted osteoblast differentiation. The exact mechanism by which SMF affects osteoblast function is not fully understood. It has been hypothesized that SMF regulates information transfer between cells and between cells and extracellular matrix through bone growth factors, and ultimately regulates gene expression and changes cell fate [30]. We examined Wnt/β-catenin signaling pathway, and MMF changed the fate of osteoblast differentiation by activating Wnt/β-catenin signaling pathway.

SMF as a non-invasive physical therapy has been used in the prevention and treatment of bone related diseases. In particular, FDA-approved pulsed electromagnetic field has being used as an effective treatment for non-union of long bones. Although electromagnetic fields work faster, SMF has the advantages of easy operation, simple power supply design, mild operation and no thermoelectric hazards. Previous studies have reported positive effects of different intensities of SMF on bone remodeling and bone metabolism in normal mice, osteoporotic mice and bone cells, including osteocytes, osteoblasts, osteoclasts and bone marrow stem cells [19,20,31–36]. One possible regulatory mechanism of SMF is related to its role in regulating systematic iron metabolism. For wild mice, MMF had little effect on iron metabolism and maintained normal physiological state. For mice with pathological states, MMF seems obliged to adjust them to the same metabolic state as normal mice. Exposed to MMF, $HAMP^{-/-}$ mice did not reduce iron absorption, either in serum or lumbar vertebra. However, MMF modifies the use of excess iron in bone tissue. MMF attenuated steap3 and DMT1 expression in the lumbar vertebra of $HAMP^{-/-}$ mice. In other words, after $HAMP^{-/-}$ mice were exposed to MMF, the excess iron in the lumbar tissue was not fully converted to labile iron, thereby reducing the oxidative state while activating the antioxidant state. The same results were obtained in the primary cell experiment *in vitro*. In primary osteoblasts, MMF activated the glutathione antioxidant system. Keap1-Nrf2 system is a common antioxidant defense mechanism [37]. When cells are stimulated by oxidative stress, the structure of Keap1 is changed, and Nrf2 is activated to translocation into the nucleus and initiate the downstream antioxidant system. In our study on the differentiation process of primary BMMs, the expression of TfR1 and steap3 decreased after exposure to MMF, while the expression of DMT1 increased. The possible reason for the different results of iron conversion in lumbar vertebra is the biological difference caused by the experimental environment *in vivo* and *in vitro*. Lumbar vertebrae continuously absorb iron from the duodenum. In vitro, although FPN of $HAMP^{-/-}$ primary mononuclear macrophages was up-regulated, no exogenous iron was added in the culture medium. The increased expression of DMT1 is due to the fact that it not only transports ferrous ions in cytoplasmic endosomes, but also acts as an iron absorption channel on the cell membrane to maintain intracellular iron homeostasis. This result indicated that the free iron in primary BMMs was increased, which could be explained by the enhancement of ROS fluorescence signal. The abnormal iron metabolism can catalyze the Fenton reaction to produce hydroxyl radicals with high reactivity, which makes the cells in a state of high oxidative stress for a long time. At the same time, the body has a set of effective antioxidant defense mechanism, so that the generation and elimination of free radicals in a dynamic balance, so as to maintain the normal physiological functions of the body. Nrf2 signaling pathway plays an important role in the body's defense against free radical oxidation. The core molecules of this signaling pathway include nuclear factor erythroid 2 related afctor 2 (Nrf2) and kelch-like ECH-associated protein 1 (Keap1). Keap1 is a specific substrate of Nrf2 and binds to the later two conserved functional domains in a 2:1 ratio. Keap1 effectively inhibits Nrf2 activity in the cytoplasm through its isolation, ubiquitination and subsequent proteomic degradation, thus ensuring that Nrf2 maintains a low level of transcriptional activity in the physiological state. When the cells are under oxidative stress, the Keap1 structure changes, resulting in the dissociation of the Keap1-Nrf2 complex. After the dissociation, Nrf2 accumulates in the cytoplasm and transfers into the nucleus, and then initiates the transcriptional expression of antioxidant enzyme genes,

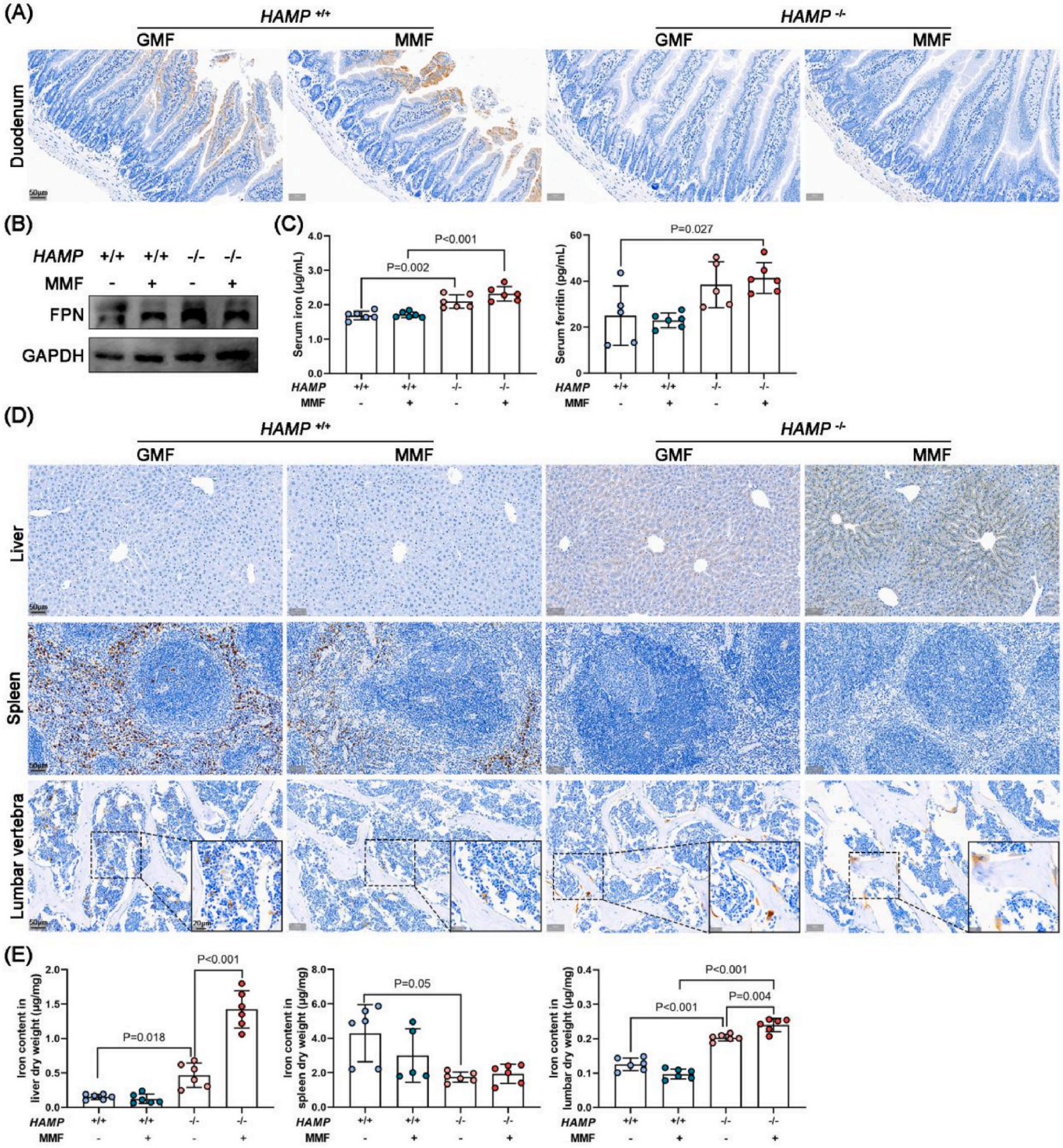

Fig. 8. Effects of MMF on iron metabolism in *HAMP*$^{+/+}$ and *HAMP*$^{-/-}$ mice. (A) Representative images of duodenal DAB Prussian blue staining (Scale bar = 50 μm). (B) Protein expression level of FPN in the duodenal. (C) The total iron content in serum was detected by AAS and serum ferritin was determined by ELISA kit. (D) Representative images of liver, spleen and lumbar vertebra DAB Prussian blue staining (Scale bar = 50 μm). (E) The total iron content in liver, spleen and lumbar vertebra were detected by AAS. Each point in the bar represents an individual animal with n = 5–6/group. (For interpretation of the references to color in this figure legend, the reader is referred to the Web version of this article.)

thus playing the role of antioxidant damage. The increased expressions of Keap1-Nrf2 and SOD1 indicated that MMF activated the antioxidant system of primary BMMs, which provided a reasonable explanation for the slower differentiation rate of macrophages into mature osteoclasts in MMF exposed group than in unexposed group. Unlike hereditary *HAMP*$^{-/-}$ mice that continuously absorb iron from the diet through the duodenum, serum ferritin is reduced in postmenopausal osteoporosis patients treated with MMF. This is undoubtedly beneficial, as serum ferritin levels in these patients are generally higher than the normal physiological levels [4]. Meaningfully, MMF increased T-scores and improved lumbar BMD in osteoporosis patients.

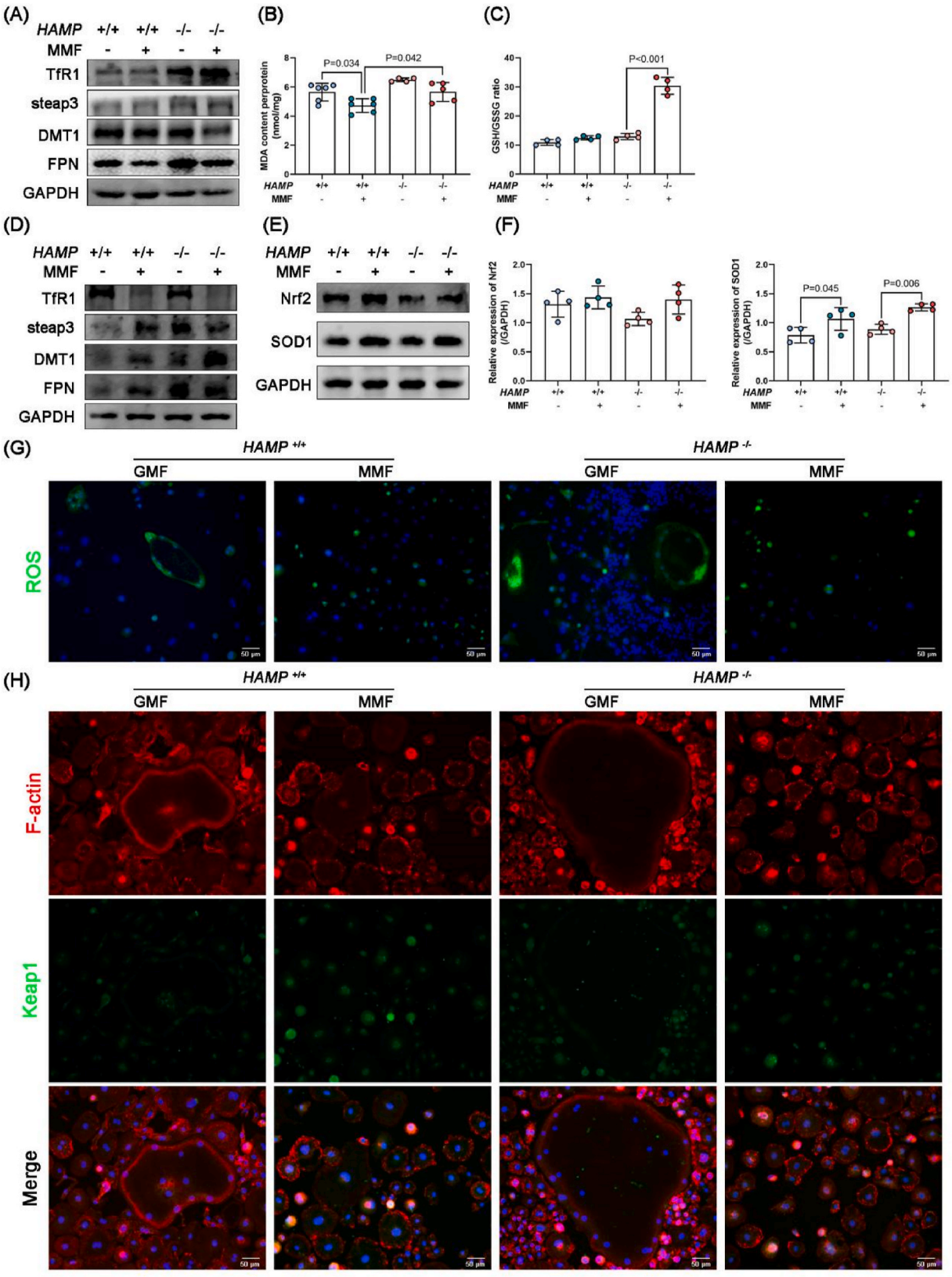

Fig. 9. Effects of MMF on REDOX status in $HAMP^{+/+}$ and $HAMP^{-/-}$ mice. (A) Protein expression level of TfR1, steap3, DMT1 and FPN in the lumbar vertebra. (B) MDA levels, (C) GSH/GSSG ratio in the lumbar vertebra of $HAMP^{+/+}$ and $HAMP^{-/-}$ mice. (D) Protein expression level of TfR1, steap3, DMT1 and FPN in primary mononuclear macrophages. (E) Protein expression level of Nrf2 and SOD1 in primary mononuclear macrophages and (F) quantitative analysis expression levels of Nrf2 and SOD1 based on western blot. (G) DCFH-DA probe labeled ROS during differentiation of primary monocytes derived from $HAMP^{+/+}$ and $HAMP^{-/-}$, Hoechst 33342 for nuclear detection (scale bar = 50 μm). (H) Immunofluorescence staining of Keap1 during differentiation of primary monocytes derived from $HAMP^{+/+}$ and $HAMP^{-/-}$, F-Actin rings of osteoclasts were detected by Alexa Fluor 555 labeled phalloidin staining and nuclei were detected by DAPI (Scale bar = 50 μm). Each point in the bar represents an individual animal or petri dish with n = 4–6/group.

5. Conclusion

In summary, the results of this study demonstrated the feasibility and potential effectiveness of MMF in the treatment of postmenopausal patients with osteoporosis and demonstrated for the first time that MMF alleviated bone loss in mice with inherited iron metabolism abnormalities. In this study, MMF exposure reduced serum ferritin in postmenopausal osteoporosis patients and which was negatively correlated with changes in lumbar BMD. Mice with hepcidin deletion (coding for *HAMP*) serve as models for iron metabolism disorders, where excessive iron uptake through the duodenum leads to chronic iron accumulation leading to bone loss. MMF increased lumbar bone mass, improved damaged bone microstructure, balanced bone turnover and improved biomechanical properties in the lumbar vertebra of $HAMP^{-/-}$ mice. In addition, MMF exposure regulates iron metabolism and antioxidant systems in the lumbar vertebra. *In vitro*, MMF exposure also inhibited osteoclastogenesis, promoted the mineralization of primary osteoblasts, and enhanced the antioxidant capacity of primary cells. Clinical trial and laboratory results suggested that MMF intervention has a protective effect against bone loss caused by iron metabolism disorders, and may be used as an alternative therapy to ameliorate osteoporosis caused by iron accumulation. We look forward to the further development and application of MMF in the treatment and prevention of iron metabolism disorders and their complications.

Author contributions

Authors' roles[1]: Study design: CZ, SW and PS. Data collection and analysis: CZ, GZ, SW and JY. Experimental platform provide: DY and PS. Drafting manuscript: CZ and CC. Revising manuscript content: all authors. Approving final version of manuscript: all authors. CZ and PS take responsibility for the integrity of the data analysis.

Declaration of competing of interest

A conflict of interest occurs when an individual's objectivity is potentially compromised by a desire for financial gain, prominence, professional advancement or a successful outcome. The Editors of the Journal of Orthopaedic Translation strive to ensure that what is published in the Journal is as balanced, objective and evidence-based as possible. Since it can be difficult to distinguish between an actual conflict of interest and a perceived conflict of interest, the Journal requires authors to disclose all and any potential conflicts of interest.

Acknowledgements

This work was supported by the National Natural Science Foundation of China (52037007), China Postdoctoral Science Foundation (2022M712599) and Heye Health Technology Chongming Project (HYCMP-2024022).

All persons who have made substantial contributions to the work reported in the manuscript (e.g., technical help, writing and editing assistance, general support), but who do not meet the criteria for authorship, are named in the Acknowledgements and have given us their written permission to be named. If we have not included an Acknowledgements, then that indicates that we have not received substantial contributions from non-authors.

Appendix A. Supplementary data

Supplementary data to this article can be found online at https://doi.org/10.1016/j.jot.2024.10.012.

References

[1] Zhang Z. Guidelines for the diagnosis and treatment of primary osteoporosis (2022). Chin J Osteoporos Bone Miner Res 2022;15(6):573–611.
[2] Jain RK, Vokes T. Dual-energy X-ray absorptiometry. J Clin Densitom 2017;20(3):291–303.
[3] Krugh M, Langaker MD. Dual-energy X-ray absorptiometry, StatPearls. StatPearls Publishing Copyright; 2024.
[4] Kim BJ, Ahn SH, Bae SJ, Kim EH, Lee SH, Kim HK, et al. Iron overload accelerates bone loss in healthy postmenopausal women and middle-aged men: a 3-year retrospective longitudinal study. J Bone Miner Res 2012;27(11):2279–90.
[5] Weinberg ED. Iron loading: a risk factor for osteoporosis. Biometals 2006;19(6):633–5.
[6] Lv Y, Zhang S, Weng X, Huang J, Zhao H, Dai X, et al. Estrogen deficiency accelerates postmenopausal atherosclerosis by inducing endothelial cell ferroptosis through inhibiting NRF2/GPX4 pathway. Faseb J 2023;37(6):e22992.
[7] Shin JA, Kim H-S, Lee Kang J, Park E-M. Estrogen deficiency is associated with brain iron deposition via upregulation of hepcidin expression in aged female mice. Neurobiol Aging 2020;96:33–42.
[8] Chen B, Wang S, Wang X, Ye J, Lu L, Gao Y, et al. Effects of deferasirox on bone mass and construction in ovariectomymice with iron accumulation.pdf. Chin J Osteoporosis & Bone Miner Res 2017;10(2):140–5.
[9] Yang J, Dong D, Luo X, Zhou J, Shang P, Zhang H. Iron overload-induced osteocyte apoptosis stimulates osteoclast differentiation through increasing osteocytic RANKL production in vitro. Calcif Tissue Int 2020;107(5):499–509.
[10] Luo C, Xu W, Tang X, Liu X, Cheng Y, Wu Y, et al. Canonical Wnt signaling works downstream of iron overload to prevent ferroptosis from damaging osteoblast differentiation. Free Radical Biol Med 2022;188:337–50.
[11] Che J, Lv H, Yang J, Zhao B, Zhou S, Yu T, et al. Iron overload induces apoptosis of osteoblast cells via eliciting ER stress-mediated mitochondrial dysfunction and p-eIF2α/ATF4/CHOP pathway in vitro. Cell Signal 2021;84:110024.
[12] Bassett C, Pawluk R, Pilla A. Augmentation of bone repair by inductively coupled electromagnetic fields. Science 1974;184(4136):575–7.
[13] Zhang G, Zhen C, Yang J, Zhang Z, Wu Y, Che J, et al. 1-2 T static magnetic field combined with Ferumoxytol prevent unloading-induced bone loss by regulating iron metabolism in osteoclastogenesis. J Orthop Translat 2023;38:126–40.
[14] Zhang K, Ge W, Luo S, Zhou Z, Liu Y. Static magnetic field promotes proliferation, migration, differentiation, and AKT activation of periodontal ligament stem cells. Cells Tissues Organs 2023;212(4):317–26.
[15] Lv H, Wang Y, Zhen C, Liu J, Chen X, Zhang G, et al. A static magnetic field improves bone quality and balances the function of bone cells with regulation on iron metabolism and redox status in type 1 diabetes. Faseb J 2023;37(7):e22985.
[16] Aydin N, Bezer M. The effect of an intramedullary implant with a static magnetic field on the healing of the osteotomised rabbit femur. Int Orthop 2010;35(1):135–41.
[17] Sun Y, Fang Y, Li X, Li J, Liu D, Wei M, et al. A static magnetic field enhances the repair of osteoarthritic cartilage by promoting the migration of stem cells and chondrogenesis. J Orthop Transl 2023;39:43–54.
[18] Yang J, Feng Y, Li Q, Zeng Y. Evidence of the static magnetic field effects on bone-related diseases and bone cells. Prog Biophys Mol Bio 2023;177:168–80.
[19] Dong D, Yang J, Zhang G, Huyan T, Shang P16T. High static magnetic field inhibits RANKL-induced osteoclast differentiation by regulating iron metabolism in Raw264.7 cells. J Tissue Eng Regen Med 2019;13(12):2181–90.
[20] Xue Y, Yang J, Luo J, Ren L, Shen Y, Dong D, et al. Disorder of iron metabolism inhibits the recovery of unloading-induced bone loss in hypomagnetic field. J Bone Miner Res 2019;35(6):1163–73.
[21] Yang J, Meng X, Dong D, Xue Y, Chen X, Wang S, et al. Iron overload involved in the enhancement of unloading-induced bone loss by hypomagnetic field. Bone 2018;114:235–45.
[22] Rupp T, Montet J, Frazer JW. A comparison of thermal and radio-frequency exposure effects on trace metal content of bloof plasma and liver cell fractions of rodents. Ann N Y Acad Sci 1975;28(247):282–91.
[23] Yang J, Zhang J, Ding C, Dong D, Shang P. Regulation of osteoblast differentiation and iron content in mc3t3-E1 cells by static magnetic field with different intensities. Biol Trace Elem Res 2018;184(1):214–25.
[24] Lesbordes-Brion J-C, Viatte L, Bennoun M, Lou D-Q, Ramey G, Houbron C, et al. Targeted disruption of the hepcidin 1 gene results in severe hemochromatosis. Blood 2006;108(4):1402–5.
[25] Nemeth E, Ganz T. Hepcidin-Ferroportin interaction controls systemic iron homeostasis. Int J Mol Sci 2021;22(12):6493.
[26] Rivera S, Nemeth E, Gabayan V, Lopez MA, Farshidi D, Ganz T. Synthetic hepcidin causes rapid dose-dependent hypoferremia and is concentrated in ferroportin-containing organs. Blood 2005;106(6):2196–9.
[27] Shen GS, Yang Q, Jian JL, Zhao GY, Liu LL, Wang X, et al. Hepcidin1 knockout mice display defects in bone microarchitecture and changes of bone formation markers. Calcif Tissue Int 2014;94(6):632–9.
[28] Li G, Zhang H, Wu J, Wang A, Yang F, Chen B, et al. Hepcidin deficiency causes bone loss through interfering with the canonical Wnt/beta-catenin pathway via Forkhead box O3a. J Orthop Translat 2020;23:67–76.
[29] Sun L, Guo W, Yin C, Zhang S, Qu G, Hou Y, et al. Hepcidin deficiency undermines bone load-bearing capacity through inducing iron overload. Gene 2014;543(1):161–5.
[30] Kim EC, Park J, Kwon IK, Lee S-W, Park S-J, Ahn S-J. Static magnetic fields promote osteoblastic/cementoblastic differentiation in osteoblasts, cementoblasts, and periodontal ligament cells. J Periodontal Implant Sci 2017;47(5):273.

[31] Yang J, Wang S, Zhang G, Fang Y, Fang Z, Shang P, et al. Static magnetic field (2–4 T) improves bone microstructure and mechanical properties by coordinating osteoblast/osteoclast differentiation in mice. Bioelectromagnetics 2021;42(3):200–11.
[32] Yang J, Zhou S, Wei M, Fang Y, Shang P. Moderate static magnetic fields prevent bone architectural deterioration and strength reduction in ovariectomized mice. IEEE Trans Magn 2021;57(7):1–9.
[33] Zhang B, Li X, Zhou X, Lou C, Wang S, Lv H, et al. Magneto-mechanical stimulation modulates osteocyte fate via the ECM-integrin-CSK axis and wnt pathway. iScience 2023;26(8):107365.
[34] Wang J, Shang P. Static magnetic field: a potential tool of controlling stem cells fates for stem cell therapy in osteoporosis. Prog Biophys Mol Bio 2023;178:91–102.
[35] Yang J, Zhang G, Li Q, Tang Q, Feng Y, Shang P, et al. Effect of high static magnetic fields on biological activities and iron metabolism in MLO-Y4 osteocyte-like cells. Cells 2021;10(12):3519.
[36] Yang J, Zhou S, Lv H, Wei M, Fang Y, Shang P. Static magnetic field of 0.2–0.4 T promotes the recovery of hindlimb unloading-induced bone loss in mice. Int J Radiat 2021;97(5):746–54.
[37] Bellezza I, Giambanco I, Minelli A, Donato R. Nrf2-Keap1 signaling in oxidative and reductive stress. BBA-Mol Cell Res 2018;1865(5):721–33.

Glossary

BV/TV: bone volume fraction
Tb.N: trabecular number
Tb.Sp: trabecular separation
Conn.D: connectivity density
Ct.Th: cortical bone thickness
Ct.Po: total porosity
Po.N: pore number
Po.V: total volume of pore space
TRAP: tartrate-resistant acid phosphatase
N.Oc/BS: osteoclast number/bone surface
Oc.S/BS: osteoclast surface/bone surface
N.Ob/BS: osteoblast number/bone surface
ALP: alkaline phosphatase
MDA: malondialdehyde
GSH: reduced glutathione
GSSG: oxidized glutathione
SOD1: superoxide dismutase 1
ΔSF: rate of serum ferritin change
ΔBMD: rate of bone mineral density change